

# ON THE STARTING REDSHIFT FOR COSMOLOGICAL SIMULATIONS: FOCUSING ON HALO PROPERTIES

Alexander Knebe<sup>1,2</sup>, Christian Wagner<sup>2</sup>, Steffen Knollmann<sup>1,2</sup>, Tobias Diekershoff<sup>2</sup>, Fabian Krause<sup>2</sup>

Draft version June 29, 2021

## ABSTRACT

We systematically study the effects of varying the starting redshift  $z_i$  for cosmological simulations in the highly non-linear regime. Our primary focus lies with the (individual) properties of dark matter halos (namely the mass, spin, triaxiality, and concentration) where we find that even substantial variations in  $z_i$  leave only a small imprint, at least for the probed mass range  $M \in [10^{10}; 10^{13}] h^{-1} M_\odot$  and when investigated at redshift  $z = 0$ . We further compare simulations started by using the standard Zel'dovich approximation to runs based upon initial conditions produced with second order Lagrangian perturbation theory. Here we observe the same phenomenon, i.e. that differences in the studied (internal) properties of dark matter haloes are practically undetectable. These findings are (for the probed mass range) in agreement with other work in the literature. We therefore conclude that the commonly used technique for setting up cosmological simulations leads to stable results at redshift  $z = 0$  for the mass, the spin parameter, the triaxiality, and the concentration of dark matter haloes.

Subject headings: galaxies: halos | cosmology: theory | cosmology: dark matter | methods: n-body simulations | methods: numerical

## 1. INTRODUCTION

During the past two decades numerical simulations of cosmic structure formation have become a standard tool in cosmology. Advances in computational algorithms combined with an ever increasing size of the machines used to run these simulations have made it possible to simulate regions of the universe with unprecedented dynamic range, recently culminating in multi-billion particle simulations of galactic halos (e.g., Stadel et al. 2008; Springel et al. 2008). However, most of the efforts towards achieving this goal have been related to refining the simulation techniques and studying the differences between various codes, respectively (cf. Frenk et al. 1999; Knebe et al. 2000; O'Shea et al. 2005; Regan et al. 2007; Heitmann et al. 2007; Agertz et al. 2007; Tasker et al. 2008). But common to all these simulations (irrespective of the applied code) is the way how the initial conditions (ICs) are generated: practically everyone in the field uses the so-called Zel'dovich approximation (Zel'dovich 1970, ZA) first employed for cosmological simulation by Klypin & Shandarin (1983) and Efsthathiou et al. (1985), despite the notion that other methods may be more suitable and accurate, respectively (e.g., Pen 1997; Sirko 2005; Hansen et al. 2007; Joyce et al. 2008). We like to remind the reader that the ZA is a first order Lagrangian perturbation theory and hence we will also refer to ZA as "1st". There are only a few parameters that require specification for this method, one of which is the starting redshift  $z_i$ ; for an elaborate discussion of (most of) the parameters in using the ICs we refer the reader to Joyce et al. (2008).

There is already a great deal of work out there related to the credibility of the ZA with respects

to transients from initial conditions (e.g. Scoccimarro 1998; Crocce et al. 2006; Tatekawa & Mizuno 2007), the memory of initial conditions (Crocce & Scoccimarro 2006), errors in real-space statistical properties of the ZA (e.g. Knebe & Domínguez 2003; Sirko 2005), discreteness effects (Baertschiger & Sylos Labini 2001; Joyce & Marcos 2007b,a) as well as descriptions of how to accurately generate multi-mass simulations (e.g. Navarro et al. 1997; Punnet et al. 2008). However, to our surprise the literature yet lacks a systematic study of the right choice for the starting redshift  $z_i$  with respects to the internal properties of dark matter halos at today's time.

On the one hand, workers in the field argue that the validity of the linear theory (upon which the ZA is based) is enforced by choosing a starting redshift in such a way that the resulting variance of the discrete density field (from now on referred to as  $\delta_B$ , see definition below) is significantly less than unity (e.g., Crocce et al. 2006; Punnet et al. 2008). But how much smaller than unity exactly? As a rule of thumb people adopted a value of  $\delta_B \approx 0.1 - 0.2$  (as pointed out by, for instance, Crocce et al. 2006; Lukic et al. 2007; Punnet et al. 2008).<sup>3</sup> But what is this choice based upon?

On the other hand, Lukic et al. (2007), for instance, provide a useful formula for estimating the starting redshift  $z_i$  based upon the requirement that the fundamental mode in the simulation box is well in the linear regime (Eq.(20) in Lukic et al. 2007); and they additionally discuss the necessity to further restrict the initial displacement of particles to a level that the first crossing of trajectories happens several expansion factors after starting the simulation (see also Valageas 2002; Crocce et al. 2006). They argue that it is important to allow for a sufficient number of expansion factors between the starting redshift and the highest redshift of physical signi-

<sup>1</sup> Departamento de Física Teórica, Módulo C-XI, Facultad de Ciencias, Universidad Autónoma de Madrid, 28049 Cantoblanco, Madrid, Spain

<sup>2</sup> Astrophysikalisches Institut Potsdam, An der Sternwarte 16, 14482 Potsdam, Germany

<sup>3</sup> Please note that these references do not argue in favour of  $\delta_B < 1$ ; they rather refer to this choice as "common practice".

cance to ensure that artifacts from the initial conditions (e.g. a regular grid structure) are lost. This goes along with the tests presented in Reed et al. (2003) where it is argued that the simulation should be evolved for at least an expansion factor of  $\sim 10$  before extracting (mass function) measurements. Starting too late (or allowing for too few expansion before extracting physical information from the simulation) will delay collapse of the first halos acting as seeds for further structure formation, e.g. the Zel'dovich approximation cannot account for shell-crossing wherein mass piles up as it flows towards overdensities (cf., Jenkins et al. 2001; Reed et al. 2003; Heitmann et al. 2008). But what is "too late"?

However, one should also not start too early to avoid numerical round-off errors and shot noise of the particles used to sample the primordial matter density field (e.g. in the case of glass ICs) (e.g., Lukic et al. 2007). The main objective of this paper is to shed light on this issue and study the differences in properties of dark matter halos at redshift  $z = 0$  when systematically varying the starting redshift  $z_i$  and consequently  $\delta_B$ .

We though have to acknowledge that this subject has in part been touched upon by other people (e.g., Jenkins et al. 2001; Reed et al. 2003; Heitmann et al. 2006; Crocce et al. 2006; Lukic et al. 2007; Tinker et al. 2008; Joyce et al. 2008). However, the primary focus of these studies was solely the mass (function) of dark matter halos and numerical effects in generating the ICs, respectively. In that regards, it has been shown by, for instance, Reed et al. (2003) that the starting redshift can have a substantial influence on the high-redshift mass function. However, such effects should have evolved away by lower redshifts since the tiny fraction of matter that is in halos at high redshift is soon incorporated into clusters or large groups (Reed et al. 2003). This is actually confirmed by the findings of Jenkins et al. (2001) who observed that the mass function at low- $z$  is not very sensitive to the starting redshift. A similar result was found by Tinker et al. (2008) for halos with mass  $M < 10^{14} h^{-1} M_\odot$ : they compared mass functions obtained with simulations based upon ZA initial conditions but variations in the starting redshift from  $z_i = 60$  to  $z_i = 35$ . However, the difference increased for halos more massive than  $10^{14} h^{-1} M_\odot$  and could become as large as 10–20%, nevertheless depending on the code and particulars of the simulation, respectively (cf. their Fig. 14). This goes along with the results of Crocce et al. (2006) who found a  $\sim 10\%$  discrepancy at  $10^{15} M_\odot$  in  $z = 0$  mass functions when comparing the standard first-order ZA with second-order Lagrangian perturbation theory (from now on referred to as "lpt2") for generating initial conditions for cosmological simulations. This may be caused by the fact that ZA assumes straight lines for particle trajectories whereas lpt2 includes the effects of gravitational tides; and the latter are most pronounced for regions containing the rarest peaks of largest height that tend to evolve into the largest galaxy clusters at low redshift (Tinker et al. 2008).

Here we extend and complement all previously mentioned studies by quantifying the impact of the initial starting redshift  $z_i$  upon the individual properties of gravitationally bound objects at redshift  $z = 0$  other than the mass alone. In addition, the same comparison is done

for simulations started by a 2nd order Lagrangian perturbation method (lpt2). This complements the research carried out by Crocce et al. (2006) who presented an in-depth investigation of transients from initial conditions in cosmological simulations in ZA and lpt2. In contrast to that study, we consider scales that are much deeper in the non-linear regime.

## 2. THE SIMULATIONS

We ran a series of simulations with the publicly available GADGET2 code. All simulations consist of  $N = 256^3$  particles in a cubical volume of  $25 h^{-1} \text{ Mpc}$  side length. The cosmology we imposed is compliant with the latest WMAP results (i.e.  $\Omega_0 = 0.28$ ;  $\Omega_m = 0.72$ ;  $h = 0.73$ ;  $\sigma_8 = 0.76$ ;  $n_s = 0.96$ ; Komatsu et al. 2008). The force resolution of our simulations is  $2 h^{-1} \text{ kpc}$ . As the phases in the generation of the ICs were identical across all models we are able to cross-compare both individual particles as well as individual halos. The latter were identified with the MPI-enabled open source halo finder AHF<sup>4</sup> (AMIGA's Halo Finder, Knebe et al. 2009), which is based upon the MHF halo finder of Gillet et al. (2004): halos are located as peaks in an adaptively smoothed density field of the simulation using an adaptive grid hierarchy based upon a refinement criterion that matches the force resolution of the actual simulation (i.e. in our case 5 particles per cell); local potential minima are computed for each of these peaks and the set of particles that are gravitationally bound to the halo are returned. For every halo we calculate a suite of canonical properties (e.g. velocity, mass, spin, shape, concentration, etc.) based upon the particles within the virial radius. The virial radius  $R_{\text{vir}}$  is defined as the point where the density profile (measured in terms of the cosmological background density  $\rho_b$ ) drops below the virial overdensity  $\rho_{\text{vir}}$ , i.e.  $M(< R_{\text{vir}}) = (4\pi R_{\text{vir}}^3 \rho_{\text{vir}}) / 3 = \rho_{\text{vir}} \rho_b$ . This threshold  $\rho_{\text{vir}}$  is based upon the dissipationless spherical top-hat collapse model and is a function of both cosmological model and time. For the given cosmology it amounts to  $\rho_{\text{vir}} = 354$  at  $z = 0$ .

We need to mention that we restricted our analysis to objects with at least 100 particles corresponding to a lower mass cut of  $M_{\text{min}} = 7.2 \cdot 10^9 h^{-1} M_\odot$  and according to the study presented in Knebe et al. (2009) we are certain that our halo catalogue is complete at this level. The total number of objects found is of order 20000 with approximately 10 objects with  $M > 10^{13} h^{-1} M_\odot$ . For a more elaborate discussion of how well our numerically determined mass functions agree with existing fitting formulae in the literature we refer the interested reader to the actual AHF paper by Knebe et al. (2009).

The simulations can be split into two distinct sets classifying the method applied to displace the particles from a regular lattice at the initial redshift  $z_i$ , i.e. using the code by Sirko (2005) we either apply

lpt1: the Zel'dovich approximation or

lpt2: 2nd order Lagrangian perturbation theory.

<sup>4</sup> AHF is already freely available from <http://www.aip.de/People/aknebe>

TABLE 1  
Simulation labels  
alongside initial  
conditions  
parameters.

run	$z_i$	box
150-lpt1	150	0.05
100-lpt1	100	0.07
050-lpt1	50	0.14
025-lpt1	25	0.28
150-lpt2	150	0.05
100-lpt2	100	0.07
050-lpt2	50	0.14
025-lpt2	25	0.28

In each of these sets we varied the starting redshift and used the values  $z_i = 150; 100; 50$ , and 25 and our convention for labelling these runs is summarized in Table 1. That table further lists the starting redshift alongside the aforementioned  $m$ s variance of the  $m$  matter distribution inside the computational volume

$$\frac{2}{B} = \frac{1}{2^2} \int_{k_{min}}^{k_{max}} P(k) k^2 dk \quad (1)$$

where  $k_{min} = 2/B$  represents the fundamental mode determined by the box size  $B$  and  $k_{max} = N^{1/3}/B$  the Nyquist frequency that additionally depends on the number of particles  $N$  used for the initial conditions.

### 3. DENSITY FIELD COMPARISON

Even though the primary focus of this study lies with the internal properties of dark matter halos (to be presented in Section 4 below) we start with an investigation of the effects of the starting redshift (and order of the Lagrangian scheme) upon the matter density field. This is due to the lack of differences found in Section 4 and we hence considered it mandatory to verify our simulations against the results obtained by other workers in the field who predominantly explored the power spectrum (and mass function of halos) in that regards.

According to the commonly accepted and applied method to generate ICs for cosmological simulations we refer to model \code{lptX-050"} as our reference model for which the  $m$ s of the matter field  $B = 0.14$  is in the commonly used range of 0.1–0.2. We therefore compare all other models in the \code{lpt1"} set) against this particular run and in analogy use \code{lpt2-050"} as the reference in the \code{lpt2"} set.

#### 3.1. Applied Comparisons

All models in a given \code{lpt1/2"} set are compared against the reference model started at  $z = 50$ . To gauge the influence of using \code{1st(lpt1/ZA)} or second order (\code{lpt2}) Lagrangian perturbation theory in the generation of the ICs we additionally cross-compare runs of these two sets against each other that started at the same redshift. In summary, this leaves us with ten comparisons summarized in Table 2.

#### 3.2. Power Spectra

We start our comparison with the power spectrum of  $m$  matter density fluctuations. The power spectrum

TABLE 2  
Applied Cross-Comparisons.

comparison	model # 1	model # 2
# 1	150-lpt1	050-lpt1
# 2	100-lpt1	050-lpt1
# 3	025-lpt1	050-lpt1
# 4	150-lpt2	050-lpt2
# 5	100-lpt2	050-lpt2
# 6	025-lpt2	050-lpt2
# 7	150-lpt1	150-lpt2
# 8	100-lpt1	100-lpt2
# 9	050-lpt1	050-lpt2
# 10	025-lpt1	025-lpt2

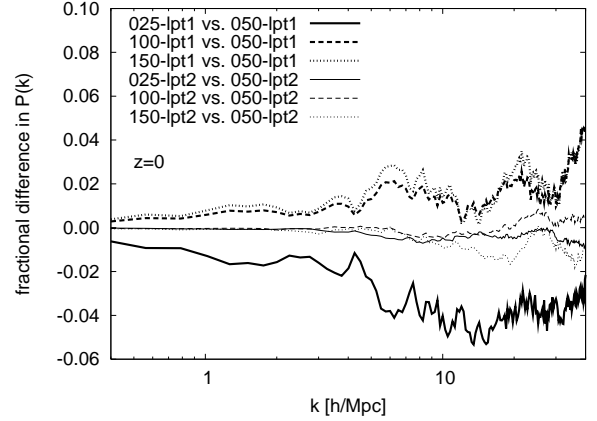


Fig. 1. Fractional difference in the power spectrum  $P(k)$  regarding the different starting redshifts at redshift  $z = 0$ . The wavenumber  $k$  ranges from the largest mode to the Nyquist frequency of the particle grid.

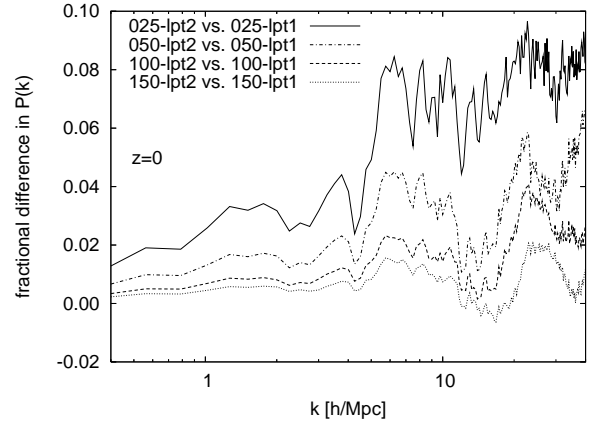


Fig. 2. Fractional difference in the power spectrum  $P(k)$  regarding the different schemes (ZA and \code{lpt2}) used to set up the initial conditions at redshift  $z = 0$ .

$$P(k) = \frac{D}{j} \frac{E}{(k)^2} ; \quad (2)$$

where  $(k)$  is the Fourier transform of the density contrast  $(\delta)$ , i.e.

$$(k) = \int \frac{d^3x}{(2\pi)^3} \exp(i\mathbf{k} \cdot \mathbf{x}) (\delta) ; \quad (3)$$

is the commonly used statistic to describe the clustering

of the density field. Here, we compute it by applying an FFT on a regular  $1024^3$  grid using the cloud-in-cell (Hockney & Eastwood 1988, CIC) scheme for the mass assignment.

We compare the power spectra of the different runs by calculating the fractional difference, e.g. in the case of "150-lpt1 vs. 050-lpt1" the fractional difference in  $P(k)$  is given by  $(P(k)_{150\text{-lpt1}} - P(k)_{050\text{-lpt1}}) / P(k)_{050\text{-lpt1}}$ .

The results for the runs started at different initial redshifts  $z_i$  with respect to the reference run started at  $z_i = 50$  (i.e., comparisons # 1 through # 6 in Table 2) are shown in Fig. 1. The thick and thin lines correspond to the ZA and lpt2 runs, respectively. We notice that the runs which were set up using the ZA differ more strongly ( $\sim 4\%$ ) when changing the respective starting redshift than the runs set up with lpt2 ( $\sim 1\%$ ). Or in other words, ICs generated using the ZA are more sensitive to the actual starting redshift (at least with respects to the power spectrum analysis) than ICs based upon lpt2. We further find, that for the ZA runs, the earlier the simulation started the more power we get at  $z = 0$  compared to the reference model started at  $z = 50$ , especially at the small-scale/high- $k$  end. Both of these results are compliant with the findings of Crocce et al. (2006) and Ma (2007). However, we like to note that given our box size and particle number we probe much smaller scales and hence a clustering regime that is highly non-linear.

In Fig. 2 we compare the power spectra of the lpt2 runs against the power spectra of the lpt1 runs for each starting redshift  $z_i$  at redshift  $z = 0$  (i.e. comparisons # 7 through # 10 of Table 2). We find that, in general, the lpt2 initial conditions lead to more power than the ZA initial conditions. Obviously, the effect is bigger the later the simulation started ( $\sim 7\%$  for  $z_i = 25$  and  $\sim 1\%$  for  $z_i = 150$ ), simply because the difference between first order and second order Lagrangian perturbation theory decreases with redshift. And again, this observation agrees with the results of other works that compared lpt1 against lpt2 (e.g. Crocce et al. 2006; Ma 2007; Nishimichi et al. 2008; Heitmann et al. 2008).

The bottom line of this sub-section therefore is that { whatever we will find in the subsequent study below { our simulations reproduce the same trends as found by others when varying either the starting redshift or the order of the Lagrangian perturbation theory, at least when it comes to studying the (power spectrum of the) matter density field.

### 3.3. Particle Positions

As all ICs were generated using the same phases we are in the advantageous position to compare individual particle positions across models. To this extent we apply two tests. The first consists of calculating the modulus of the difference between those positions

$$|r_j - r_i| = |x_i - x_j| \quad (4)$$

where  $x_i$  is the position in simulation  $i$  and  $x_j$  in simulation  $j$ , and the second utilizes the so-called density cross-correlation coefficient.

In Fig. 3 we show for our set of comparisons (cf. Section 3.1) the position difference  $|r_j - r_i|$  (in units of the force resolution, i.e.  $2h^{-1}$  kpc) for 1% of particles randomly se-

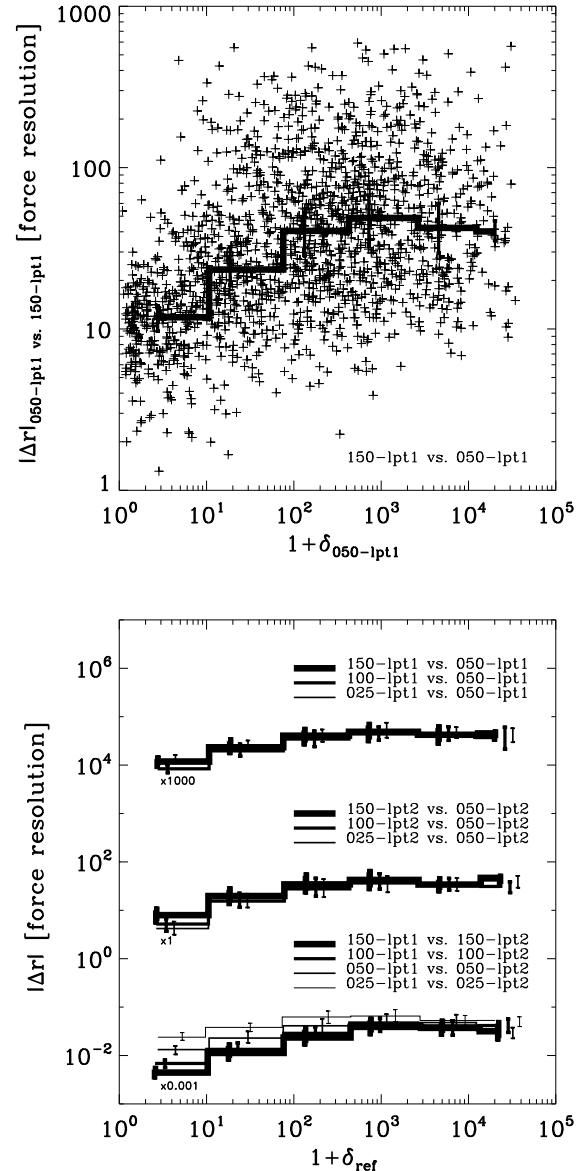


Fig. 3. | Deviation (normalized to the force resolution) of particle coordinates at  $z = 0$ . The upper panel presents a random sample of 1% of all particles alongside the median  $|r|$  in six bins in  $1 + \delta_{\text{ref}}$ . The lower panel only shows the medians multiplied by 100, 1, and 0.01, respectively, to avoid crowding.

lected from the total number of particles as a function of density as measured at the position of the particle<sup>5</sup> in the reference model started at redshift  $z_i = 50$  (i.e. 050-lpt1 and 050-lpt2, respectively) and hence labelled  $_{050\text{-lpt1}}$  in the upper panel and  $_{\text{ref}}$  in the lower panel. The upper panel shows the actual scatter plot for one particular comparison (i.e., 050-lpt1 vs. 150-lpt1) together with the median while the lower panel shows only the medians of  $|r|$  in six logarithmically spaced bins. Note that the whole particle set has been used to calculate the medians and to avoid crowding in the figures we multiplied

<sup>5</sup> The density contrast  $\delta = (\rho - \bar{\rho}) / \bar{\rho}$  has first been calculated by assigning the mass of each particle to a regular grid of size  $512^3$ . Then the grid values have been interpolated back to the particles' positions.

TABLE 3  
Cross-correlation coefficients.

comparison	L = 32 <sup>3</sup>	L = 64 <sup>3</sup>	L = 128 <sup>3</sup>	L = 256 <sup>3</sup>	L = 512 <sup>3</sup>
150- $\text{pt1}$ vs. 050- $\text{pt1}$	0.9853	0.9452	0.8755	0.7487	0.6800
100- $\text{pt1}$ vs. 050- $\text{pt1}$	0.9867	0.9487	0.8839	0.7599	0.6882
025- $\text{pt1}$ vs. 050- $\text{pt1}$	0.9851	0.9232	0.8758	0.7477	0.6637
150- $\text{pt2}$ vs. 050- $\text{pt2}$	0.9861	0.9424	0.8690	0.7566	0.6833
100- $\text{pt2}$ vs. 050- $\text{pt2}$	0.9872	0.9461	0.8749	0.7650	0.6911
025- $\text{pt2}$ vs. 050- $\text{pt2}$	0.9874	0.9462	0.8758	0.7662	0.6932
150- $\text{pt1}$ vs. 150- $\text{pt2}$	0.9889	0.9523	0.8856	0.7732	0.6982
100- $\text{pt1}$ vs. 100- $\text{pt2}$	0.9879	0.9503	0.8808	0.7659	0.6914
050- $\text{pt1}$ vs. 050- $\text{pt2}$	0.9851	0.9518	0.8673	0.7447	0.6793
025- $\text{pt1}$ vs. 025- $\text{pt2}$	0.9808	0.8824	0.8484	0.7175	0.6380

the medians by 100, 1, and 0.01, respectively. The error bars represent the 25<sup>th</sup> and 75<sup>th</sup> percentiles (slightly shifted for each model along the x-axis for clarity).

We notice the expected trend for  $\langle r_j \rangle$  to increase with increasing density contrast, i.e. the differences across models are more pronounced in high-density regions. We now checked (though not shown here) that the differences are never larger than the virial radii of the halos these particles reside in. However, the observed trend is expected: the origin of these deviations is the dynamical instability of particle trajectories in the high-density regions (e.g. Knebe et al. 2000; Valluri et al. 2007). As is well known, the trajectories within virialized systems tend to be chaotic and any small differences existing at any time moment will tend to grow very fast with time. The divergence can thus be expected to be more important in non-linear regions and this explains the trend of larger  $\langle r \rangle$ 's in denser regions. The differences in the low-density regions are substantially smaller, but still larger than the force resolution and hence considered physical. However, when investigating underdense regions  $1+ < 1$  we notice that the median of  $\langle r_j \rangle$  "saturates" at approximately the level of 10 force resolution and hence denotes the level that marks them in minimum expectation for the position difference.

We also observe that the medians do not show considerable variations when changing the starting redshift. Further, the trend for  $\langle r_j \rangle$  to increase with  $\{$  that appears to be independent of  $z_i \{$  is also of comparable strength for  $\text{pt1}$  and  $\text{pt2}$ .

However, when comparing  $\text{pt1}$  against  $\text{pt2}$  there appears to be a drift towards smaller particle position differences (in low-density regions) when moving to higher starting redshifts. This is readily explained by the fact that at higher redshifts the differences between  $\text{pt1}$  and  $\text{pt2}$  vanish. Nevertheless, this trend is far less pronounced in high-density regions. We conclude that the differences in  $P(k)$  as seen in Fig. 2 therefore stem from rather low-density regions.

We also cross-compared an earlier started model to a later started one at its actual starting redshift, e.g. a snapshot of run 150- $\text{pt1}$  at redshift  $z = 50$  to the ICs of simulation 050- $\text{pt1}$ . We though chose to not show the results as all differences in the positions  $\langle r_j \rangle$  are smaller than the force resolution and we hence consider them unphysical.

We like to caution the reader that this particular test of

investigating the spatial differences  $\langle r_j \rangle$  does not provide us with the information which method is better or worse. It simply shows that the differences in the initial matter distribution are practically all at the same level, irrespective of starting redshift and order of the Lagrangian perturbation theory used. There is a trend for differences in the particles' position to increase in high-density regions but this trend is the same for cross-comparisons of the  $\text{pt1}$ ,  $\text{pt2}$  and  $\text{pt1}$  vs.  $\text{pt2}$  models, respectively.

As a second quantitative measure of differences we construct the so-called cross-correlation coefficient (Coles et al. 1993; Splinter et al. 1998; Knebe et al. 2000)

$$K = \frac{h_{ij}}{\sigma_i \sigma_j}; \quad (5)$$

where  $i$  and  $j$  specify the different simulations and the average is taken over the computational box.

To compute  $K$ , we have calculated the densities  $\rho_i; \rho_j$  on a regular mesh using the triangular-shaped cloud (Hockney & Eastwood 1988, TSC) density assignment scheme, and then used the resulting density field to compute  $h_{ij}$  as well as the corresponding variances  $\sigma_i$  and  $\sigma_j$ . We have varied the size of the grid in order to show the dependence of the cross-correlation on the smoothing scale of the density field.

The results are shown in Table 3 where it is obvious that in all cases the cross-correlation worsens for smaller smoothing scales (larger grid sizes). This is compliant with the trends seen in Fig. 3, i.e. that  $\langle r_j \rangle$  increases with  $\{$ : the smaller the smoothing, the smaller structures are resolved in the density field. The degraded cross-correlation therefore indicates that there are differences in locations and/or densities of these small-scale structures. If we restrict the correlation analysis to a coarse grid, we smooth the particle distribution with a fairly large smoothing length and smear out the details and differences in the small-scale structure.

But nevertheless, the absolute values of  $K$  are of the same order when contrasting different comparisons. One may additionally argue that  $K$  is slightly higher for the  $\text{pt2}$  vs.  $\text{pt2}$  cross-correlations than for the corresponding  $\text{pt1}$  vs.  $\text{pt1}$  case indicative of the higher order of the  $\text{pt2}$  scheme, which is in agreement with our findings for the power spectra (cf. Fig. 1). Further  $\{$  as in the case of the power spectra (cf. Fig. 2)  $\{$  the cross-correlations for  $\text{pt1}$  vs.  $\text{pt2}$  become smaller for earlier starting redshifts,

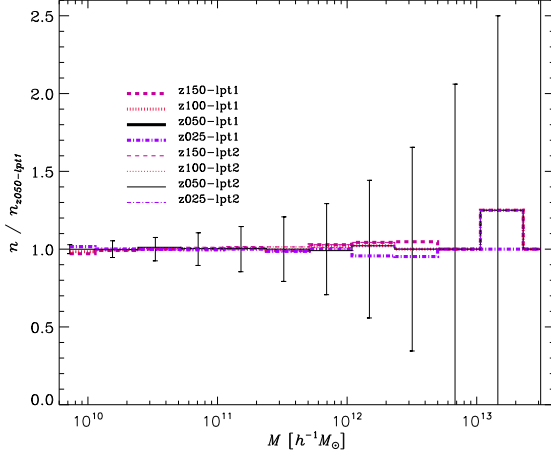


Fig. 4. | Ratio of the mass function at redshift  $z = 0$  of gravitationally bound objects for all eight models to the respective reference model started at  $z = 50$ . The (Poissonian) error bars measure the  $3\sigma$  variance.

e.g. applying a  $256^3$  grid the  $K$  value for 150-lpt1 vs. 150-lpt2 is 8% higher than for 025-lpt1 vs. 025-lpt2. This is exactly the same value as we find for the difference of the two power spectra at the corresponding wave number (i.e. the Nyquist frequency).

We also like to note that the value of the density cross-correlation coefficient  $K$  found here is of the same order as for a comparison of the same simulation run with different codes under matching conditions (cf. Table 2 in Knebe et al. 2000).

In summary, we do observe differences in the particle positions when changing either the starting redshift or the order of the Lagrangian perturbation theory. And these differences are obviously more pronounced in high-density regions where particle trajectories appear to be more "chaotic". However, trends for these differences to change with starting redshift are at best marginal, irrespective of lpt1 or lpt2.

#### 4. HALO COMPARISON

The same model comparisons as in the previous section (cf. Table 2) are now going to be performed using the halo catalogues obtained via the halo finder AHF (cf. Section 2). In that regards we will focus on four quantities, namely the mass  $M$ , the triaxiality (Franx et al. 1991)

$$T = \frac{a^2 - b^2}{a^2 - c^2} \quad (6)$$

where  $a > b > c$  are the eigenvalues of the moment of inertia tensor, the spin parameter (Bullock et al. 2001)

$$S = \frac{L}{2 M V R} \quad (7)$$

where  $L$  is the absolute value of the angular momentum,  $M$  the halo mass,  $R$  its radius, and  $V^2 = GM/R$ , and finally the concentration

$$c = \frac{R}{R_2} \quad (8)$$

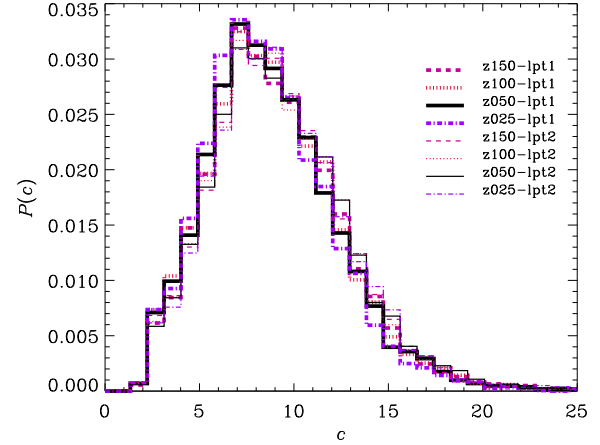
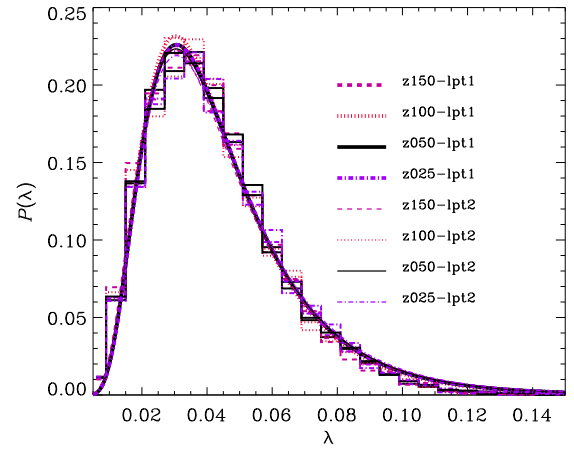
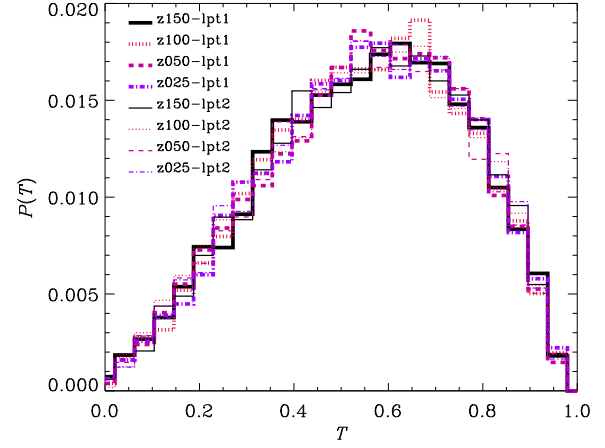


Fig. 5. | Probability distribution of the triaxiality parameter  $T$  (top), the spin parameter (middle), and the concentration  $c$  (bottom) for all models.

where  $R_2$  measures the point where  $r^2 \rho(r)$  peaks, with  $\rho(r)$  representing the spherically averaged density profile.

##### 4.1. Distributions

We start with inspecting the distribution functions for the four quantities under investigation. For the mass function  $n(>M)$  we decided to plot the ratios with respects to the reference model started at  $z_1 = 50$  whereas

TABLE 4  
Best-fit parameters  
for the spin  
parameter  
distributions.

run	0	0
150-lpt1	0.040	0.509
100-lpt1	0.039	0.501
050-lpt1	0.040	0.507
025-lpt1	0.040	0.506
150-lpt2	0.039	0.524
100-lpt2	0.040	0.515
050-lpt2	0.040	0.513
025-lpt2	0.040	0.519

for  $P(T)$ ,  $P(\epsilon)$ , and  $P(c)$  we chose to plot the actual distributions. The results can be viewed in Figs. 4 and 5.

The dependence of the mass function on the starting redshift has already been investigated by several groups before (e.g., Jenkins et al. 2001; Reed et al. 2003; Crocce et al. 2006; Lukic et al. 2007; Tinker et al. 2008).

Our own results can be viewed in Fig. 4 where we plot the ratio of the mass function of a particular model and the fiducial 050-lpt1/2 run; the (Poissonian) error bars measure the  $3\sigma$  variance and are hence proportional to  $3 \sqrt{N_{\text{halos}}^{\text{bin}}}$  where  $N_{\text{halos}}^{\text{bin}}$  is the average number of halos in the respective bin.

The (lack of) differences seen in Fig. 4 is consistent with the outcome of similar studies in the field (e.g. Jenkins et al. 2001; Reed et al. 2003; Crocce et al. 2006; Lukic et al. 2007; Tinker et al. 2008): most of the previous investigations focussed on the very high-mass end of the mass function, i.e.  $10^{14} - 10^{15} h^{-1} M$  and found transients to be important there. However, that mass regime is not probed by our simulations; we are analysing halos within a mass range for which none of the previously mentioned papers have found any differences either.

The limited influence of the starting redshift upon (low-mass) dark matter halos at redshift  $z = 0$  can also be observed for the shape, spin parameter, and concentration presented in Fig. 5: there are hardly any noticeable differences in the distributions when changing  $z_i$ . This figure is accompanied by Table 4 for which the spin parameter distributions have been fitted to a lognormal distribution

$$P(\epsilon) = \frac{1}{\epsilon} \exp\left(-\frac{\ln^2(\epsilon/\epsilon_0)}{2\sigma^2}\right); \quad (9)$$

with the two best-fit parameters  $\epsilon_0$  and  $\sigma$  listed in Table 4. We again note that they are practically indistinguishable, irrespective of the model and the starting redshift  $z_i$ . However, we note that the width of the distribution as measured by  $\sigma$  appears to be marginally smaller in the lpt1 set.

Our results from this section indicate that the starting redshift has practically no influence on today's attributes of dark matter halos (at least not for the properties analysed here, namely the mass, the spin parameter, the triaxiality, and the concentration and for objects within the given mass range  $10^{10} - 10^{13} h^{-1} M$ ). And the same holds for the order of the Lagrangian perturbation theory, i.e. whether lpt1 or lpt2 is used to generate the ICs

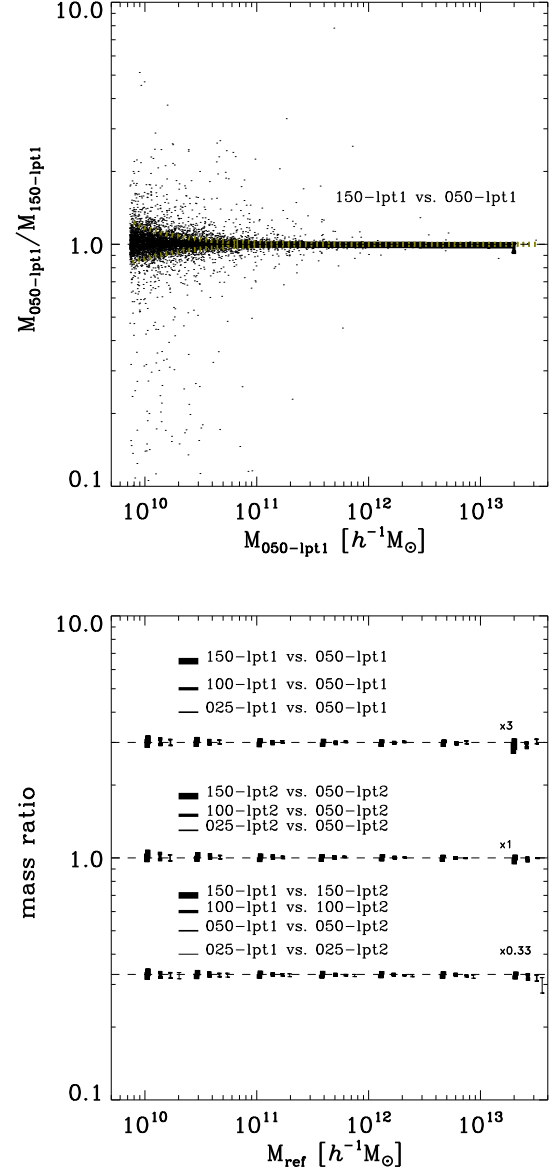


Fig. 6. | Cross-correlation of the mass  $M_{\text{vir}}$  of individual halos. The upper panel presents a random sample of 1% of all particles alongside the median mass ratio in six bins in  $M_{\text{ref}}$ . We further show the curves for mass ratio stemming from differences in the number of particles of 20 as dashed curves. The lower panel only shows the 25<sup>th</sup> and the 75<sup>th</sup> percentiles as bars around the medians multiplied by 3, 1, and 1/3, respectively, to avoid crowding.

has no effect on the particulars of halos at redshift  $z = 0$ .

#### 4.2. Cross-Correlations

As the simulations were started with identical phases we could use the particle IDs to establish a mapping between two different simulations. This has been applied in Section 3.3 where we presented a direct comparison of individual particles (e.g., the spatial difference  $\mathbf{r}_j$ ). But if we plan to do the same for the halos, we require a more sophisticated technique to uniquely cross-identify halos amongst different simulations. To this extent we utilize a tool that comes with the AHF package and is called MergerTree. Originally it serves the purpose of

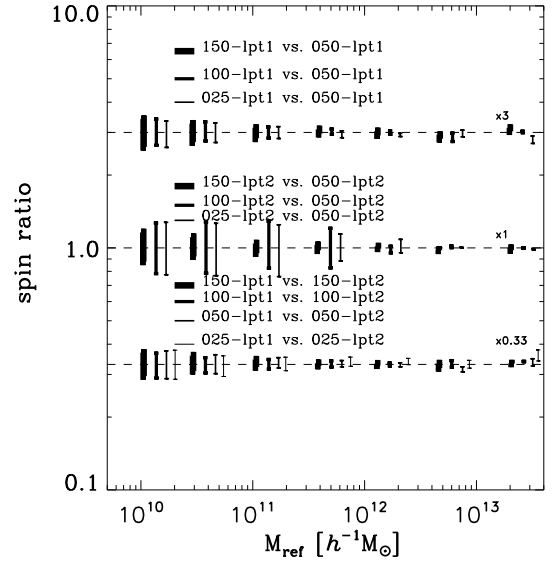
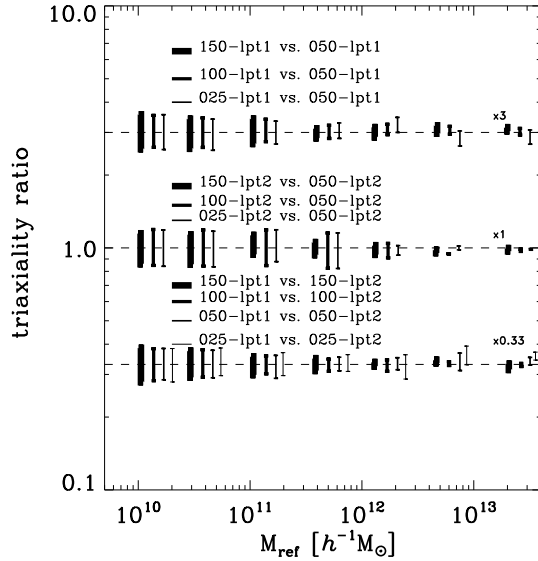
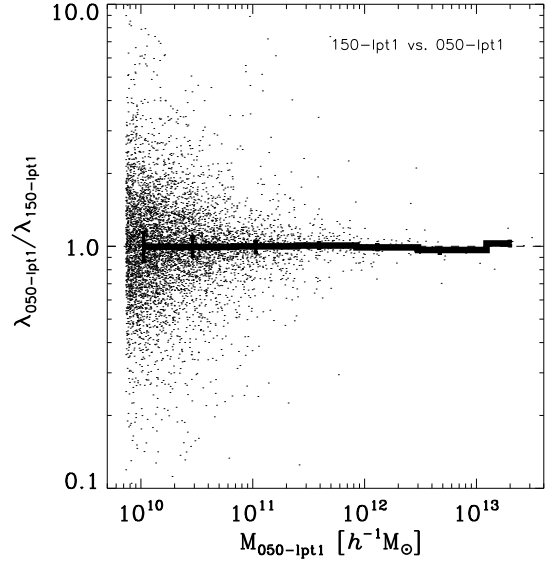
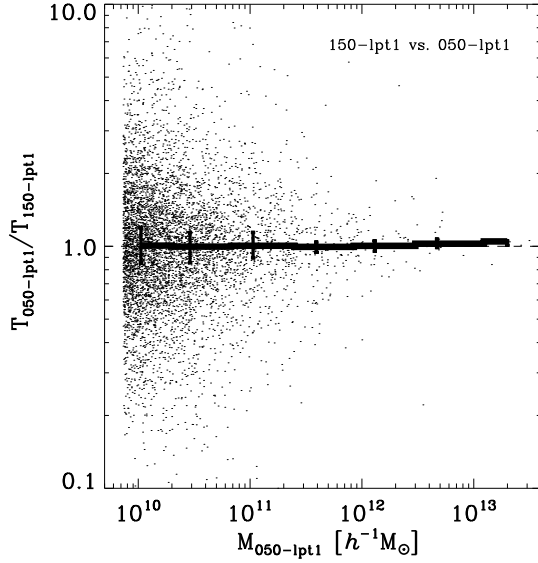


Fig. 7.] Cross-correlation of the triaxiality parameter  $T$  of individual halos. The same logic for the panels is used as in Fig. 6.

Fig. 8.] Cross-correlation of the spin parameter of individual halos. The same logic for the panels is used as in Fig. 6.

identifying corresponding objects in the same simulation at different redshifts (and hence the name MergerTree). But it can also be applied to simulations of different models run with the same initial phases for the initial conditions like in our case. The MergerTree cross-correlation is done by linking objects that share the most common particles and has been successfully applied to similar comparisons before (e.g. Knebe et al. 2006).

We consider again mass  $M$ , triaxiality  $T$ , spin parameter  $\lambda$ , and concentration  $c$  and the results can be found in Figs. 6-9 where we plot the ratio of said quantities to the reference model against the mass  $M$  in that reference model. As in Fig. 3 we present in the upper panel the actual scatter plot for 1% of the particles alongside the median in seven bins while the lower panel this time only shows the range from the 25<sup>th</sup> to the 75<sup>th</sup> percentile (centered about the median multiplied by 3, 1, and 1/3,

respectively) marginally shifted for each model on the x-axis for clarity.

We note that (the medians of) the ratios in all instances are consistent with unity. The error bars (representing 50% of the halos) are well concentrated around unity, in particular in the case of the mass ratio, and do not vary strongly with halo mass. We though observe that the individual scatter about that median (cf. upper panels) increases with decreasing halo mass; as a matter of fact, the ratio can become substantially large (of order two for the mass and order ten for the shape/spin) for the lowest mass objects. However, we attribute this to the differences in the particle positions (in high-density regions and hence in and about halos) already noted in Fig. 3. And as shown in Knollmann & Knebe (2009), tiny variations in the particle positions lead to different density contours upon which the halo finding algorithm

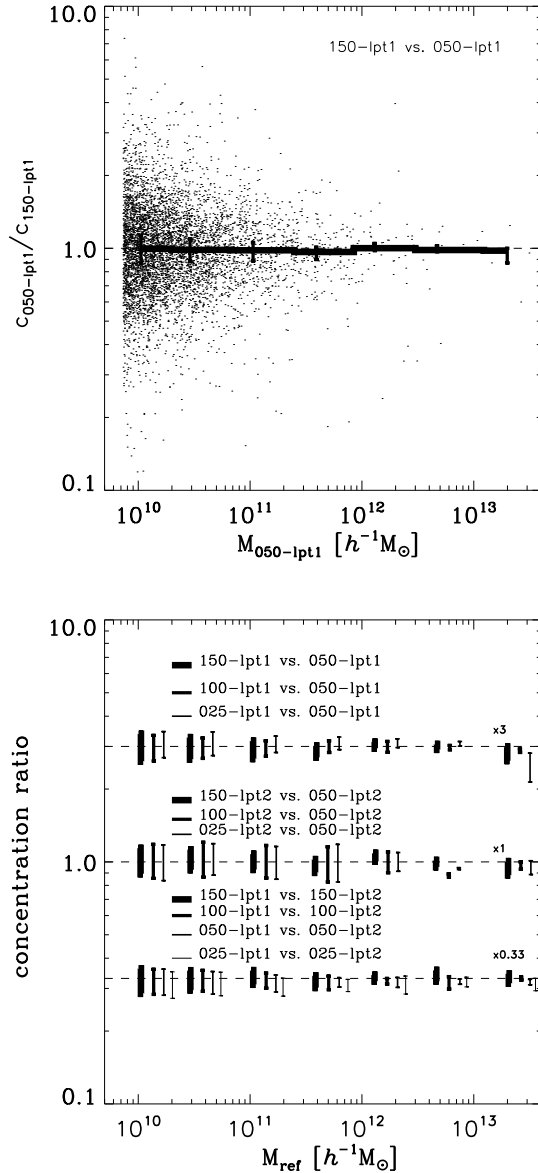


Fig. 9. | Cross-correlation of the concentration  $c$  of individual halos. The same logic for the panels is used as in Fig. 6.

of AHF is based. This then entails marginal differences in the halo properties that become more apparent at the low mass end where halos only consist of few particles. To better gauge this explanation we also plot in Fig. 6 as dashed lines those curves that mark a difference in particle number by 20; and we observe that most of the ratios lie between these curves.

The result of this section is rather remarkable as the ratio of properties of cross-identified halos is always consistent with unity, even if the starting redshift is as small as  $z_i = 25$ . The observed scatter about unity increases at the lower mass end which is naturally explained by variations in the number of particles making up the actual halo and hence is rather a peculiarity of the halo finding algorithm (Kneibmann & Kneibmann 2009). However, the variation of the median as indicated by the error bars in the lower panels of Figs. 6 & 9 clearly shows that the me-

dians are consistent with unity.

We are therefore confident that while there are one-to-one variations the statistical properties of halos are unaffected by the starting redshift (cf. Section 4.1). This result is again extended to the order of the Lagrangian perturbation theory used for generating the ICs. While we still found remnants from transients in the power spectrum (cf. Fig. 2) and deviations of particle positions (cf. Fig. 3) no effects are observed for individual properties of dark matter halos at redshift  $z = 0$  anymore.

## 5. CONCLUSIONS AND DISCUSSION

We performed a systematic study of varying the starting redshift  $z_i$  for cosmological simulations. We further used two methods to generate the ICs, namely the Zel'dovich approximation (a first order Lagrangian perturbation method) and an explicit second order Lagrangian perturbation code. The resulting snapshots at redshift  $z = 0$  were analysed with respects to properties of the matter density field as well as the statistical and individual properties of dark matter halos. Besides of (expected) fluctuations in high-density regions and at the low-mass end of the halo population the differences are rather marginal. On average, the objects have indistinguishable properties irrespective of the starting redshift. Surprisingly, even the simulation started as late as  $z_i = 25$  for which the rms matter fluctuations are  $\sigma_B = 0.28$  and hence larger than the commonly adopted value of  $0.1 - 0.2$  gave comparable results to the dual model started at  $z_i = 50$ . For the probed mass range  $M \in [10^{10}; 10^{13}] h^{-1} M_{\odot}$ , we conclude that (at least at low redshift  $z = 0$ ) the starting redshift has little (if any) influence on the (statistical) properties of the halo population. Or in other words, the resulting halo properties of mass  $M < 10^{13} h^{-1} M_{\odot}$  at redshift  $z = 0$  are stable against reasonable variations in the rms matter fluctuations  $\sigma_B$  and hence the starting redshift  $z_i$ . We note that our results are in agreement with the findings presented throughout the literature where differences have only been found on scales  $M > 10^{14} h^{-1} M_{\odot}$  (e.g., Jenkins et al. 2001; Reed et al. 2003; Heitmann et al. 2006; Crocce et al. 2006; Lukic et al. 2007; Tinker et al. 2008; Joyce et al. 2008).

We further found that also the order of the Lagrangian perturbation theory used to generate the ICs is of little relevance. While it leaves an imprint on the matter distribution (especially the power spectrum) the study of gravitationally bound objects at redshift  $z = 0$  is hardly affected, at least when it comes to the spin parameter  $\lambda$ , the triaxiality  $T$ , and the concentration  $c$ . This result actually goes along with the arguments presented by Reed et al. (2003), i.e. the effects of a "wrong" starting redshift should have evolved away by lower redshifts since the tiny fraction of matter that is in halos at high redshift is soon incorporated into clusters or large groups. This explains why Jenkins et al. (2001) as well as Tinker et al. (2008) did find that the (low- $z$ ) mass function is not very sensitive to the starting redshift.

One concern that may be raised with respects to our results is the size of our simulation box and finite volume effects, respectively. We concede that the amplitude of fluctuations at the size of the box is of order unity at redshift  $z = 0$  and therefore couplings to modes on even larger scales are missing. While this certainly

affects the halo mass function and the power spectrum. We though argue that our primary results are not influenced. If we were to adjust our mass functions for such finite volume effects using the recipes outlined in, for instance, Reed et al. (2007), Lukic et al. (2007), or Power & Knebe (2006) we would need to apply the same correction to all our models. But as we only compare models amongst each other our findings should not be contaminated by such a systematic change. In addition, we showed in a previous study that the influence of large-scale modes upon the properties of dark matter haloes at redshift  $z = 0$  will lead to differences in, for instance, the spin parameter of order  $< 15\%$  with the concentration being hardly affected at all (Power & Knebe 2006).

We further acknowledge that our analysis focused on simulations primarily analysed at redshift  $z = 0$ . And our results are not as surprisingly as one may initially think as at this time the scales under consid-

eration are deeply in the non-linear regime and the memory of the initial conditions should have been lost (Crocce & Scoccimarro 2006). At earlier times the situation may be different which explains the results of others who found a dependence of the high-mass of the multiplicity function especially at high redshift (e.g. Reed et al. 2003; Crocce et al. 2006; Lukic et al. 2007; Tinker et al. 2008). We leave a more in-depth investigation of this (using higher resolution simulations) to a future study.

AK is supported by the MICINN through the Ramon y Cajal programme. AK and SRK acknowledge funding through the Emmy Noether programme of the DFG (KN 755/1). The simulations and the analysis presented in this paper were carried out on the Sanssouci cluster at the Astrophysikalisches Institut Potsdam.

## REFERENCES

- Agertz, O., Moore, B., Stadel, J., Potter, D., Miniati, F., Read, J., Mayer, L., Gawryszczak, A., Kuvshinov, A., Nordlund, A., Pearce, F., Quilis, V., Rudd, D., Springel, V., Stone, J., Tasker, E., Teyssier, R., Wadsley, J., & Walker, R. 2007, *MNRAS*, 380, 963
- Baertschiger, T., & Sylos Labini, F. 2001, *ArXiv Astrophysics e-prints*
- Bullock, J. S., Dekel, A., Kolatt, T. S., Kuvshinov, A. V., Klypin, A. A., Porciani, C., & Primack, J. R. 2001, *ApJ*, 555, 240
- Coles, P., Meltott, A. L., & Shandarin, S. F. 1993, *MNRAS*, 260, 765
- Crocce, M., Pueblas, S., & Scoccimarro, R. 2006, *MNRAS*, 373, 369
- Crocce, M., & Scoccimarro, R. 2006, *Phys. Rev. D*, 73, 063520
- Efstathiou, G., Davis, M., White, S. D. M., & Frenk, C. S. 1985, *ApJS*, 57, 241
- Frax, M., Illingworth, G., & de Zeeuw, T. 1991, *ApJ*, 383, 112
- Frenk, C. S., White, S. D. M., Bode, P., Bond, J. R., Bryan, G. L., Cen, R., Couchman, H. M. P., Evrard, A. E., Gnedin, N., Jenkins, A., Kuvshinov, A. M., Klypin, A., Navarro, J. F., Norman, M. L., Ostriker, J. P., Owen, J. M., Pearce, F. R., Pen, U.-L., Steinmetz, M., Thomas, P. A., Villumsen, J. V., Wadsley, J. W., Warren, M. S., Xu, G., & Yepes, G. 1999, *ApJ*, 525, 554
- Gill, S. P. D., Knebe, A., & Gibson, B. K. 2004, *MNRAS*, 351, 399
- Hansen, S. H., Agertz, O., Joyce, M., Stadel, J., Moore, B., & Potter, D. 2007, *ApJ*, 656, 631
- Heitmann, K., Lukic, Z., Fasel, P., Habib, S., Warren, M. S., White, M., Ahrens, J., Ankeny, L., Armstrong, R., O'Shea, B., Ricker, P. M., Springel, V., Stadel, J., & Trac, H. 2007, *ArXiv e-prints*, 706
- Heitmann, K., Lukic, Z., Habib, S., & Ricker, P. M. 2006, *ApJ*, 642, L85
- Heitmann, K., White, M., Wagoner, C., Habib, S., & Higdon, D. 2008, *ArXiv e-prints*
- Hockney, R. W., & Eastwood, J. W. 1988, *Computer simulation using particles* (Bristol: Hilger, 1988)
- Jenkins, A., Frenk, C. S., White, S. D. M., Colberg, J. M., Cole, S., Evrard, A. E., Couchman, H. M. P., & Yoshida, N. 2001, *MNRAS*, 321, 372
- Joyce, M., & Marcos, B. 2007a, *Phys. Rev. D*, 76, 103505
- 2007b, *Phys. Rev. D*, 75, 063516
- Joyce, M., Marcos, B., & Baertschiger, T. 2008, *ArXiv e-prints*, 805
- Klypin, A. A., & Shandarin, S. F. 1983, *MNRAS*, 204, 891
- Knebe, A., & Domínguez, A. 2003, *Publications of the Astronomical Society of Australia*, 20, 173
- Knebe, A., Domínguez, A., & Domínguez-Tenreiro, R. 2006, *MNRAS*, 371, 1959
- Knebe, A., Kuvshinov, A. V., Gottlober, S., & Klypin, A. A. 2000, *MNRAS*, 317, 630
- Knollmann, S., & Knebe, A. 2009, *ApJ*, in press, 0, 0
- Komatsu, E., Dunkley, J., Nolte, M. R., Bennett, C. L., Gold, B., Hinshaw, G., Jarosik, N., Larson, D., Limon, M., Page, L., Spergel, D. N., Halpern, M., Hill, R. S., Kogut, A., Meyer, S. S., Tucker, G. S., Weiland, J. L., Wollack, E., & Wright, E. L. 2008, *ArXiv e-prints*, 803
- Lukic, Z., Heitmann, K., Habib, S., Bashinsky, S., & Ricker, P. M. 2007, *ApJ*, 671, 1160
- Ma, Z. 2007, *ApJ*, 665, 887
- Navarro, J. F., Frenk, C. S., & White, S. D. M. 1997, *ApJ*, 490, 493
- Nishimichi, T., Shirata, A., Taruya, A., Yahata, K., Saito, S., Suto, Y., Takahashi, R., Yoshida, N., Matsubara, T., Sugiyama, N., Kaya, I., Jing, Y., & Yoshikawa, K. 2008, *ArXiv e-prints*
- O'Shea, B. W., Nagamine, K., Springel, V., Hemquist, L., & Norman, M. L. 2005, *ApJS*, 160, 1
- Pen, U.-L. 1997, *ApJ*, 490, L127+
- Power, C., & Knebe, A. 2006, *MNRAS*, 370, 691
- Prunet, S., Pichon, C., Aubert, D., Pogosyan, D., Teyssier, R., & Gottlober, S. 2008, *ApJS*, 178, 179
- Reed, D., Gardner, J., Quinn, T., Stadel, J., Fardal, M., Lake, G., & Governato, F. 2003, *MNRAS*, 346, 565
- Reed, D. S., Bower, R., Frenk, C. S., Jenkins, A., & Theuns, T. 2007, *MNRAS*, 374, 2
- Regan, J. A., Hahnelt, M. G., & Viel, M. 2007, *MNRAS*, 374, 196
- Scoccimarro, R. 1998, *MNRAS*, 299, 1097
- Sirko, E. 2005, *ApJ*, 634, 728
- Splinter, R. J., Meltott, A. L., Shandarin, S. F., & Suto, Y. 1998, *ApJ*, 497, 38
- Springel, V., Wang, J., Vogelsberger, M., Ludlow, A., Jenkins, A., Heitmann, K., Navarro, J. F., Frenk, C. S., & White, S. D. M. 2008, *ArXiv e-prints*, 809
- Stadel, J., Potter, D., Moore, B., Diemand, J., Madau, P., Zemp, M., Kuhlen, M., & Quilis, V. 2008, *ArXiv e-prints*, 808
- Tasker, E. J., Brunino, R., Mitchell, N. L., Michielsen, D., Hopton, S., Pearce, F. R., Bryan, G. L., & Theuns, T. 2008, *ArXiv e-prints*, 808
- Tatekawa, T., & Mizuno, S. 2007, *Journal of Cosmology and Astro-Particle Physics*, 12, 14
- Tinker, J., Kuvshinov, A. V., Klypin, A., Abazajian, K., Warren, M., Yepes, G., Gottlober, S., & Holz, D. E. 2008, *ApJ*, 688, 709
- Valageas, P. 2002, *A & A*, 385, 761
- Valluri, M., Vass, I. M., Kazantzidis, S., Kuvshinov, A. V., & Bohn, C. L. 2007, *ApJ*, 658, 731
- Zeldovich, Y. B. 1970, *A & A*, 5, 84